Materials Horizons

ROYAL SOCIETY OF CHEMISTRY

COMMUNICATION

View Article Online
View Journal

Cite this: DOI: 10.1039/d6mh00220j

Received 4th February 2026,
Accepted 23rd March 2026

DOI: 10.1039/d6mh00220j

rsc.li/materials-horizons

Scalable, low-cost ink-based processing of high-performance silver selenide thermoelectrics

Md. Omarsany Bappy, [ab] Guoyue Xu, [a] Kaidong Song, [a] Qiang Jiang, [a] Paribesh Acharyya, [c] Berardo Matalucci, [d] Allen Gray, [d] Mercouri Kanatzidis, [c] Tengfei Luo [a] and Yanliang Zhang *[a]

The growing global energy demand and its accelerating contribution to climate change emphasize the urgent need for sustainable energy conversion/harvesting technologies. Thermoelectric (TE) devices offer a compelling route to directly convert waste heat into electricity and enable solid-state cooling without moving parts or harmful refrigerants. Achieving their full potential requires not only higher TE performance (zT) but also scalable, low-cost manufacturing processes. Here, we introduce a transformative ink-based processing approach for scalable manufacturing of high-performance silver selenide-based TE materials and devices. Using a simple, high-throughput ink-mixing and blade coating strategy, our Ag_2Se-based materials under the optimized composition and processing conditions yield an ultrahigh room-temperature power factor of 2.8 mW m^{-1} K^{-2}, over 100% higher than baseline samples and a reproducible figure of merit zT of 1 at room temperature. A thermoelectric generator (TEG) achieves a very competitive power density of 112 mW cm^{-2} at a 90 °C temperature difference between the hot and cold sides of the device, which is among the highest reported for silver selenide-based TE devices to date. This facile, scalable ink-based processing establishes a practical pathway toward industrial-scale manufacturing and widespread adoption of thermoelectric devices, advancing sustainable energy technologies.

New concepts

Over 60% of world energy consumption is lost as waste heat, while global energy demand and carbon emissions continue to rise. Technologies that can reclaim this wasted energy or provide efficient, emission-free cooling are urgently needed. Thermoelectrics offer a promising solid-state energy harvesting and cooling solution, but their widespread adoption has been limited by high material costs and complex fabrication routes in traditional manufacturing processes. This work presents an innovative scalable ink-based processing strategy that enables low-cost and high-performance thermoelectric materials and devices. By transforming silver and selenide elemental powders into printable inks and engineering a blade-coated manufacturing route, we demonstrate both competitive material performance and one of the highest power densities reported for silver-selenide-based thermoelectric generators. The scalable, versatile, and low-cost ink processing strategy demonstrated here directly addresses the key barriers preventing thermoelectric devices from reaching practical, industrial-scale deployment. The results highlight a realistic pathway toward affordable thermoelectric systems that can contribute meaningfully to global energy sustainability, waste-heat recovery, and environmentally friendly cooling technologies.

Introduction

Thermoelectric devices (TEDs) are solid-state energy converters that convert thermal energy into electricity when subjected to an external temperature gradient or generate a temperature difference and cooling effect when provided with electric current.[1] Thermoelectric generators (TEGs) have very broad industrial applications in waste heat recovery and distributed power generation to improve energy efficiency and resilience, as well as energy harvesting to power widespread sensors and the Internet of Things.[2,3] Thermoelectric coolers (TECs) offer environmentally friendly and emission-free solid-state cooling without the need of any refrigerant or moving parts, which are very advantageous in energy-efficient and localized cooling of electronics, medical devices, automobiles, data centers, and buildings.[4] Thus, thermoelectric technologies have garnered significant attention due to their immense potential for enabling energy harvesting and solid-state emission-free cooling.[1,5–8]

The efficiency of thermoelectric materials is governed by the dimensionless figure of merit, $zT = S^2\sigma T/(\kappa_l + \kappa_e)$, where S denotes the Seebeck coefficient, σ the electrical conductivity, T the absolute temperature, and κ_l and κ_e represent the lattice and electronic contributions to the thermal conductivity respectively.[9,10] Optimization of S, σ, and κ requires simultaneous control of electron and phonon transport properties, and

[a] Department of Aerospace and Mechanical Engineering, University of Notre Dame, Notre Dame, IN 46556, USA. E-mail: yzhang45@nd.edu
[b] Department of Mechanical Engineering, Bangladesh University of Engineering and Technology, Dhaka, 1000, Bangladesh
[c] Department of Chemistry, Northwestern University, Evanston, IL 60208, USA
[d] MIMiC Systems Inc., Brooklyn, NY 11205, USA

achieving high zT requires sophisticated design and manufacturing of electron transmitting and phonon blocking structures to maximize the power factor $S^2\sigma$ while reducing the κ.[9,11]

Among different types of thermoelectric materials, bismuth telluride-based alloys continue to dominate room-temperature thermoelectrics, yet n-type materials still exhibit zT values at or below unity.[9,11–14] The shortage of tellurium motivates the development of Te-free thermoelectrics. Over the past decades, numerous chalcogenides have been explored for high zT.[15] Silver selenide (Ag_2Se), a narrow-bandgap n-type chalcogenide, is an ideal candidate for room-temperature applications due to its high power factor and intrinsically low thermal conductivity.[12,16–19] It exhibits a stable orthorhombic (β) structure at temperatures below 130 °C[20] and thus most studies focus on its near-room-temperature behavior where it achieves improved zT.[21]

Despite advances in zT, the absence of scalable, low-cost synthesis and fabrication methods remains a key barrier to widespread thermoelectric deployment.[22–25] Traditionally, film-based thermoelectric devices have been fabricated *via* physical or chemical deposition, magnetron sputtering, and the vacuum thermal co-evaporation method.[26–29] These methods are limited by complex multi-step procedures, high equipment costs, and significant environmental waste. Other methods, like vacuum filtration, offer poor thickness control, limited design flexibility, and reduced performance when films are integrated into devices.[12,30] On the other hand, ink-based deposition techniques including blade coating, screen printing, aerosol-jet printing, extrusion printing, and inkjet printing provide scalable, cost-effective control over thermoelectric device geometry and structure, with the potential to revolutionize their fabrication.[11,16,31–36] Recent ink-based printing of BiTe and AgSe-based thermoelectrics has achieved room-temperature zT values near 1, comparable to bulk materials produced by conventional methods.[11,12,16,32,34,37–39] Among ink-based processing techniques, blade coating stands out for its low cost, scalability, and minimal material waste, making it ideal for both film-based and bulk devices.[11,34]

Here, we demonstrate an ink-based processing approach (Fig. 1A) to fabricate thick AgSe films and bulk structures, achieving a room-temperature power factor of 2.8 mW m^{-1} K^{-2}, among the highest reported n-type thermoelectrics made by ink-based approach (Fig. 1B).[12,16,28–30,35,36,40,41] The ink formulation, synthesis and sintering conditions were optimized to maximize the power factor. Bayesian optimization (BO) machine-learning techniques offered a principled framework to determine the optimal stopping point for these iterative optimizations.[11,12,34] The optimized sample with excess selenium exhibits a zT of 1 at room temperature, over 90% higher than that of the baseline sample (defined as the samples sintered and synthesized together at 200 °C, Fig. S1). A unicouple device is demonstrated for energy harvesting, which produces an ultrahigh normalized power density of 0.14 W m^{-2} K^{-2} at a 90 °C temperature gradient, representing one of the highest values reported in literature (Fig. 1C).[12,28–30,35,36,40–43] Achieving high power factor, zT and high device performances through a simple, scalable manufacturing route offers transformative potential for producing thermoelectric devices with the maximum performance at the minimum cost, enabling widespread applications in sustainable energy harvesting and solid-state, refrigerant-free cooling.

Results and discussion

Optimization of ink composition and processing parameters

AgSe samples were fabricated *via* the blade coating method involving three key steps: ink preparation, template-assisted blade coating, and post-processing. This approach is scalable to produce both thick films and bulk pellets. The ink, comprising Ag and Se particles, DI water, xanthan gum, and Disperbyk-110 binder, was systematically optimized by tuning constituent ratios to maximize the power factor. The Ag : Se ratio was systematically optimized, as it critically governs carrier concentration and resulting TE properties.[44] The binder promoted particle surface interactions, enabling uniform film formation. Following blade coating, the samples underwent drying, cold pressing, synthesis, and sintering in a tube furnace, which increased density and improved electrical conductivity. Cold pressing was carried out at 25 MPa for 10 min, based on optimized conditions established in our previous work.[34] Following cold pressing, the samples were synthesized and sintered at different temperatures guided by the literature (Fig. S1).[11,16,40,41,45] Despite the presence of porosity, the samples sintered at 350 °C (Fig. S1) exhibited the highest electrical conductivity, accompanied by a reduced Seebeck coefficient and a moderate power factor. Sintering at 350 °C, well above the selenium melting point (~220 °C), leads to selenium loss, resulting in porosity and a reduced Seebeck coefficient. Additional selenium was added to the Ag_2Se to offset selenium loss. Previous studies have shown that adding a small amount of excess selenium significantly enhances the power factor.[44] The additional selenium substantially boosts carrier mobility while preventing the emergence of the metastable phase.[12] We therefore synthesized silver selenide with selenium enrichment to achieve the highest power factor. To minimize porosity, the synthesis and sintering steps were performed separately. The Ag_2Se samples were first synthesized, then cold pressed, and finally sintered (Fig. S2). The ink composition, synthesis, and sintering conditions were systematically optimized to maximize the power factor (Fig. S3 and S4), as they critically govern the composition, microstructure, and performance of the films. With 9% excess selenium, a synthesis temperature of 350 °C for 90 min, and sintering temperature of 375 °C for 60 min, the highest power factor of 2.8 mW m^{-1} K^{-2} was achieved (Fig. S4). Fig. S5 shows the Seebeck coefficient, electrical conductivity, and power factor, along with the microstructure of the optimized samples at intermediate process steps. To validate the maximum power factor, further optimization was performed using Gaussian process regression (GPR) coupled with Bayesian optimization. The GPR model, trained on synthesis, sintering, and ink parameters, accurately predicted a maximum power factor of 2.73 mW m^{-1} K^{-2} (Fig. S6 and Tables S1, S2), within the uncertainty of the experimentally achieved 2.8 mW m^{-1} K^{-2}. The expected improvement from Bayesian Optimization (BO) was minimal near these conditions, confirming the final composition and processing parameters are optimal within the

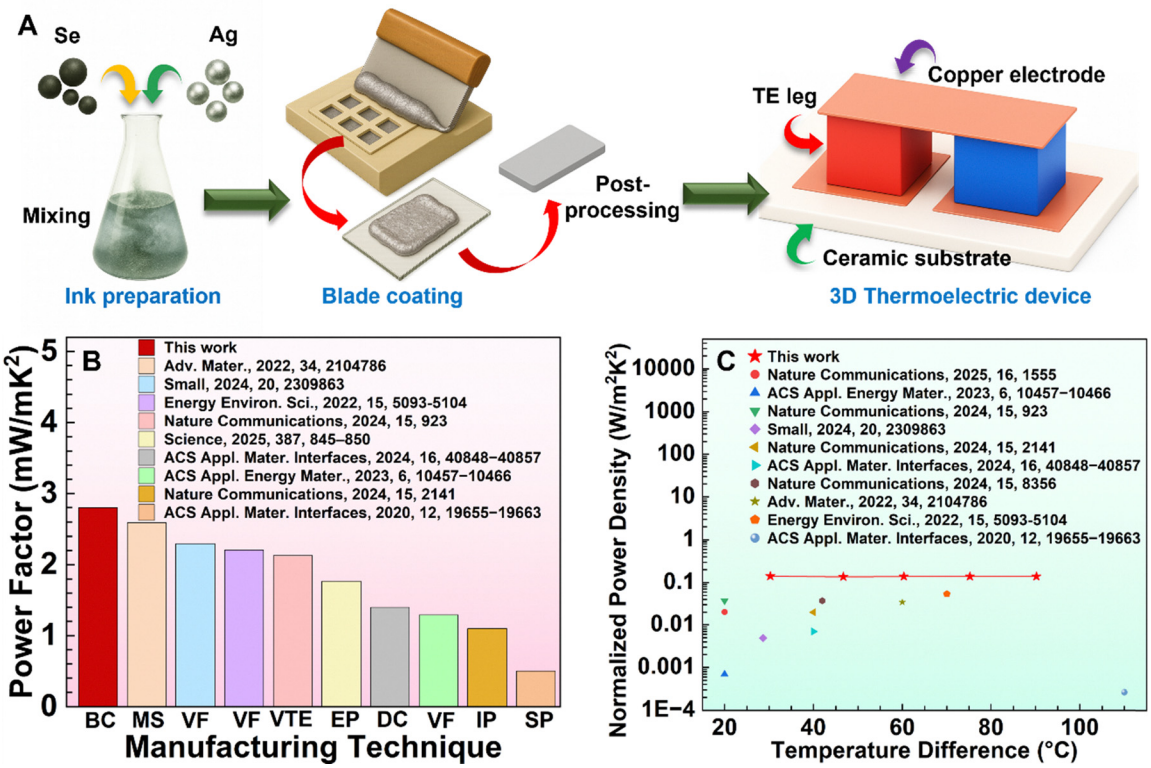

Fig. 1 (A) Schematic illustration of the AgSe thermoelectric ink preparation and blade coating method for thermoelectric materials and device fabrication. (B) Comparison of room-temperature power factor of blade-coated AgSe reported here *vs.* AgSe prepared by other methods from the literature (BC – Blade coating, MS – Magnetron sputtering, VF – Vacuum filtration, VTE – vacuum thermal co-evaporation, EP – Extrusion printing, DC – Drop casting, IP – Inkjet printing, and SP – Screen printing).[12,16,28–30,35,36,40,41] (C) Comparison of normalized output power density of the thermoelectric generator fabricated in this work with AgSe-based devices reported in the literature.[12,28–30,35,36,40–43]

explored design space. The BO analysis validated that the experimental maximum was achieved under these constrained conditions, as no higher power factor was identified.

Microstructure analysis

To elucidate the processing–structure–property relationships in blade-coated samples, we carried out a detailed microstructural analysis. Scanning electron microscopy (SEM) revealed the sample morphology, while energy-dispersive X-ray spectroscopy (EDS) confirmed the composition. X-ray diffraction (XRD) identified a predominantly orthorhombic Ag_2Se phase in both optimized and baseline samples, providing a structural basis for their thermoelectric performance. Fig. 2A shows the X-ray diffraction (XRD) patterns, where both the baseline and optimized samples reveal diffraction peaks that match the standard Ag_2Se phase (Reference code: 96-223-0973), suggesting high crystallinity and purity. Notably, the optimized sample shows sharper and well-defined peaks, indicating improved crystallinity. The absence of peaks corresponding to elemental silver (Ag) or selenium (Se) confirms the complete formation of Ag_2Se in both samples.

The SEM images in Fig. 2B and C illustrate distinct microstructural features of the baseline (unpolished top) and optimized (unpolished top) samples respectively. The baseline sample (Fig. 2B) shows a more granular surface with porosities, while the optimized sample (Fig. 2C) has a smoother, more uniform morphology. The pores in unoptimized samples likely arise from solvent evaporation during drying and can coalesce into larger voids during extended heating in the synthesis and sintering process. The optimized samples exhibit negligible porosity, a result of separating the synthesis and sintering steps. Most solvents are removed during the drying and synthesis stages, and subsequent cold pressing after synthesis further densifies the material, minimizing pore formation. Fig. 2D presents the SEM image of the optimized sample (polished cross-section), showing a dense morphology with $<7\%$ porosity. Further insights into the elemental composition of the optimized sample are provided by EDS mapping in Fig. 2E, which highlights the uniform distribution of silver (Ag) and selenium (Se) across the sample. Fig. S7 shows the EDS elemental mapping along the polished cross-section of the optimized sample, confirming the uniform distribution of all constituent elements. SEM–EDS mapping of the as-fabricated silver-selenide films confirms the Ag:Se molar ratio of approximately 2:1. The sample at optimized synthesis and sintering conditions exhibits a $\sim 9\%$ lower Se atomic concentration compared to the initial ink due to selenium loss during the synthesis and sintering steps.[46] The combination of XRD, SEM, and EDS data demonstrates that the optimized Ag_2Se sample exhibits superior crystallinity, reduced porosity, and enhanced elemental homogeneity,

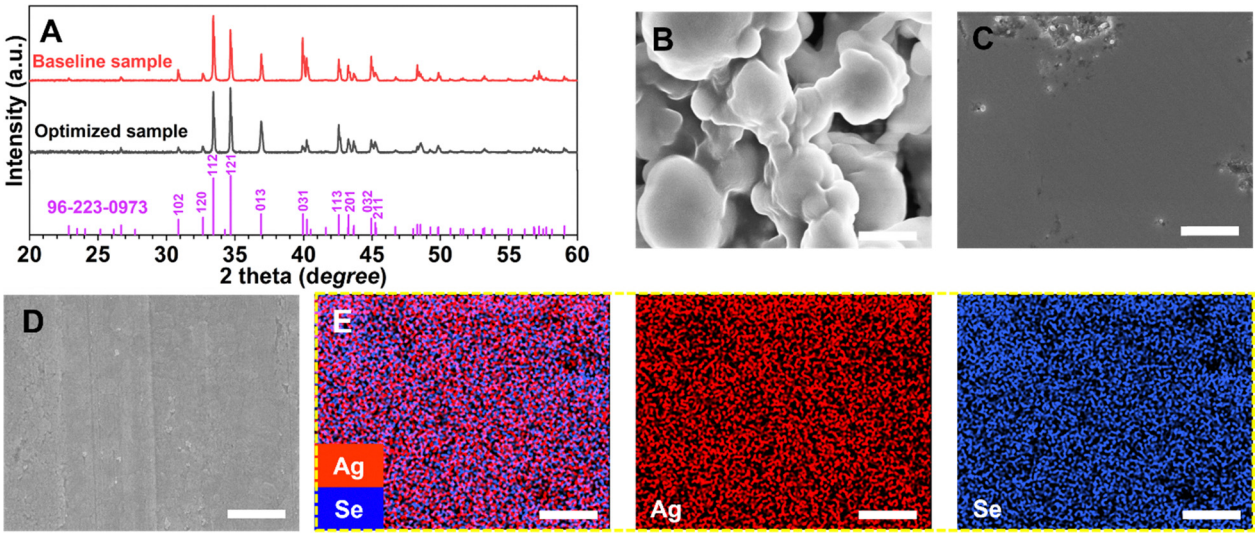

Fig. 2 (A) X-ray diffraction results of the optimized and baseline silver selenide sample. The reference XRD pattern at the bottom corresponds to standard Ag_2Se (Reference code: 96-223-0973). Scanning electron microscopy (SEM) images of the (B) baseline sample (unpolished top), (C) optimized sample (unpolished top), and (D) optimized sample (polished cross-section). (E) Energy dispersive X-ray spectrometry (EDS) elemental mapping of the optimized Ag_2Se sample (unpolished top, corresponding to Fig. 2C). Scale bar 1 μm.

which are likely to contribute to improved charge carrier mobility and overall thermoelectric performances.

Thermoelectric properties

Fig. 3 shows the thermoelectric transport properties of the silver selenide samples. Under optimized synthesis and sintering conditions, samples containing 9% excess selenium exhibited the highest power factor. The Seebeck coefficient increased from -135.3 μV K^{-1} in the composition with no excess selenium to a peak value of -153.3 μV K^{-1} with 9% excess selenium, while the electrical conductivity increased concurrently from 1002 to 1174 S cm^{-1} (Fig. 3A). This enhancement correlates with the increased carrier mobility from 1790 cm^2 V^{-1} s^{-1} in the baseline sample to 2330 cm^2 V^{-1} s^{-1} in the optimized sample. The simultaneous enhancement of both parameters leads to a substantial increase in the power factor from 1.84 to 2.8 mW m^{-1} K^{-2} (Fig. 3B), underscoring the critical role of selenium enrichment in optimizing charge carrier transport properties. The addition of a small amount of excess selenium serves two important roles. First, it compensates for selenium loss during synthesis and sintering, helping maintain the stoichiometry of Ag_2Se and suppress the formation of metastable or defect-rich phases. The improved compositional stability leads to enhanced crystallinity as evidenced by the sharper XRD peaks (Fig. 2). Second, it improves the sintering and densification due to the relatively low melting point of selenium, leading to reduced porosity. Together, these compositional and structural improvements enhance Seebeck coefficient and carrier mobility. Fig. 3C and D present the temperature-dependent thermoelectric properties of blade-coated Ag_2Se films sintered at 375 °C. A peak power factor of 3.08 mW m^{-1} K^{-2} is obtained at 110 °C due to a significant increase of electrical conductivity with temperature despite a small decrease of Seebeck coefficient.

The room-temperature thermal diffusivity of both baseline and optimized samples was measured using the Ångström method (Fig. S8). Thermal conductivity was calculated as $k = \alpha\rho C_p$, where k, α, ρ, and C_p denote the thermal conductivity, thermal diffusivity, density, and specific heat of the sample. Measured density is 7040 kg m^{-3}, and C_p value was taken from previously published literature.[47] The optimized sample exhibited a thermal conductivity of 0.85 W m^{-1} K^{-1}, compared to 0.75 W m^{-1} K^{-1} for the baseline sample, yielding a room-temperature zT of 1, representing a 90% improvement over the baseline zT of 0.52. To assess reproducibility, four batches (each batch containing at least four samples) of Ag_2Se were prepared under identical conditions, yielding a highly consistent room temperature power factor with a standard deviation $<5\%$ (Fig. S9 and Table S3).

Device performances

To demonstrate the performance of the printed silver selenide materials, a unicouple device (TE leg dimension is 1.5 mm × 1.5 mm × 1.5 mm) was fabricated. Fig. S10 shows the schematic illustration of the thermoelectric device fabrication process. The n-type Ag_2Se leg reported in this study and the p-type leg (here we used BiSbTe-based materials as the p-type leg) were integrated electrically in series and thermally in parallel. A ~300 nm layer of Ni and a ~50 nm layer of Au was deposited on the thermoelectric legs and then bonded to the copper electrodes using Bi/Sn solder.

The inset of Fig. 4A shows the photograph of the fabricated device. Power-generation performances were measured under a hot-side temperature ranging from ~48 °C to ~115 °C, while the cold-side temperature increased from 18 °C to 24 °C. The device generates an open-circuit voltage of 32.7 mV (Fig. 4A) under a 90 °C temperature gradient and delivers over 5 mW

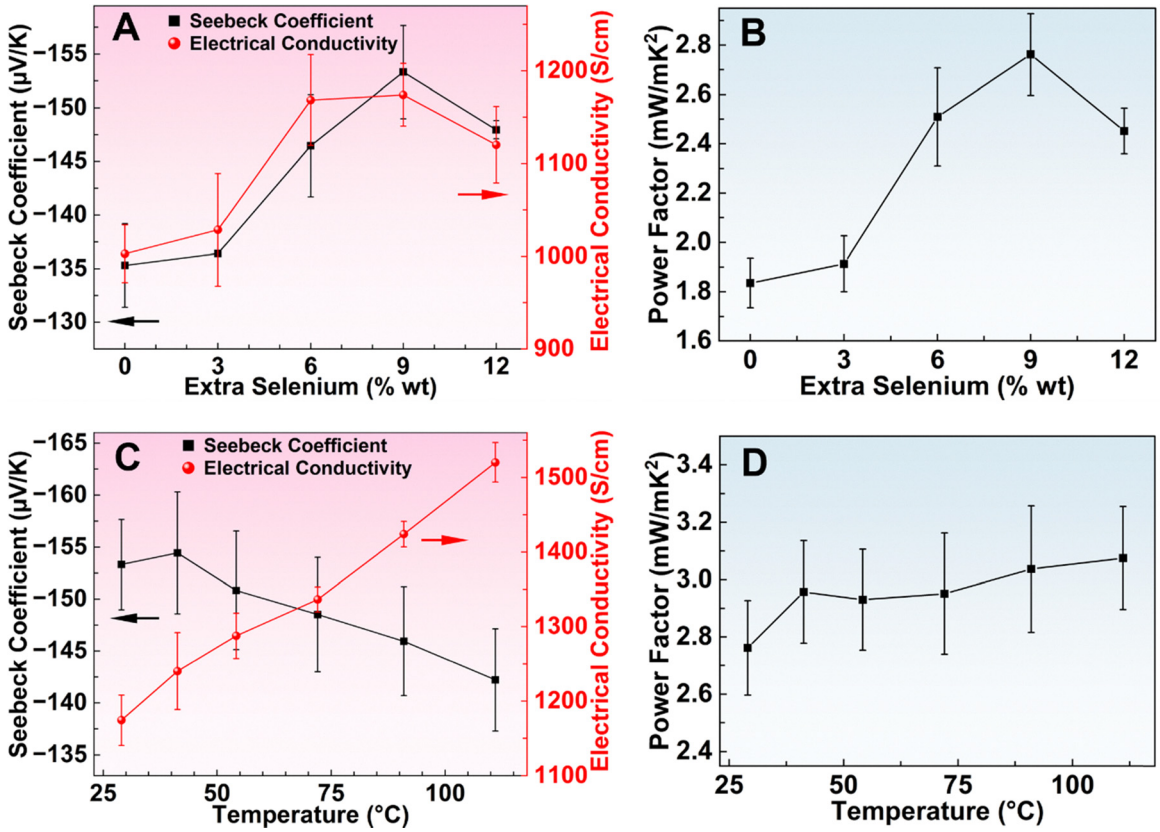

Fig. 3 Room temperature thermoelectric properties of the silver selenide samples: (A) Seebeck coefficient and electrical conductivity, (B) power factor as a function of extra selenium concentrations. Temperature-dependent thermoelectric properties: (C) Seebeck coefficient, and electrical conductivity, (D) power factor. Each point represents the average value and the error bar represents the standard deviation of at least four samples.

power and draws >0.3 A current when the external load matches the device resistance (Fig. 4B and C). The TEG delivers a peak power density of 112 mW cm^{-2} (Fig. 4D), placing it among the highest reported for printed thermoelectric devices (Fig. 1C).[12,28–30,35,36,40–43] Power density was calculated by normalizing the output power to the thermoelectric leg's cross-sectional area. Further optimization of the electrical contact between the thermoelectric legs and copper electrodes could significantly enhance device performances.

Conclusion

In conclusion, we report a highly scalable, low-cost ink-based manufacturing process to produce silver selenide with exceptional thermoelectric performances, alongside the demonstration of a fully printed thermoelectric device for energy harvesting. The optimized Ag_2Se materials deliver a power factor of 2.8 mW m^{-1} K^{-2} and a competitive zT of 1 at room-temperature. The unicouple device delivers an output power density of 112 mW cm^{-2} at a temperature difference of 90 °C, demonstrating the promise of ink-based processing for scalable device fabrication. Beyond these advances, our strategy offers a generalizable framework for ink-based fabrication of a wide range of high-performance and low-cost materials and devices for broad applications in energy conversion and storage and thermal management.

Materials and methods

Materials

Silver powder (particle size 2–3.5 μm, ≥99.9% trace metals basis), selenium powder (particle size ~149 μm, ≥99.5% trace metals basis), deionized (DI) water (industrial grade), and xanthan gum were obtained from Sigma-Aldrich. Disperbyk-110 was procured from BYK Inc.

Ink processing, blade coating, and post-processing

In a typical ink processing procedure, a shear-thinning solvent was prepared by dissolving xanthan gum and Disperbyk-110 binder in deionized (DI) water. Thermoelectric ink was then formulated by mixing thermoelectric particles with the solvent in a sealed container using a planetary mixer (AR-100) at 650 rpm for 30 min, with stainless steel balls added to improve dispersion (the solid particles contain silver and selenium. The ratio of solid particle to solvent is 20 : 80. The solvent consists of 0.7% xanthan gum, 1.2% Disperbyk-110, and 98.1% water). Cuboid-shaped samples (13 mm × 3 mm × 0.5 mm) were fabricated on flexible polyimide substrates using a PDMS-template-assisted blade coating method (Fig. 1A). The PDMS template was cast, cleaned with isopropyl alcohol (IPA), treated with oxygen plasma (Harrick Plasma Cleaner, PDC-001-HP), and aligned onto a plasma-cleaned polyimide substrate. Thermoelectric

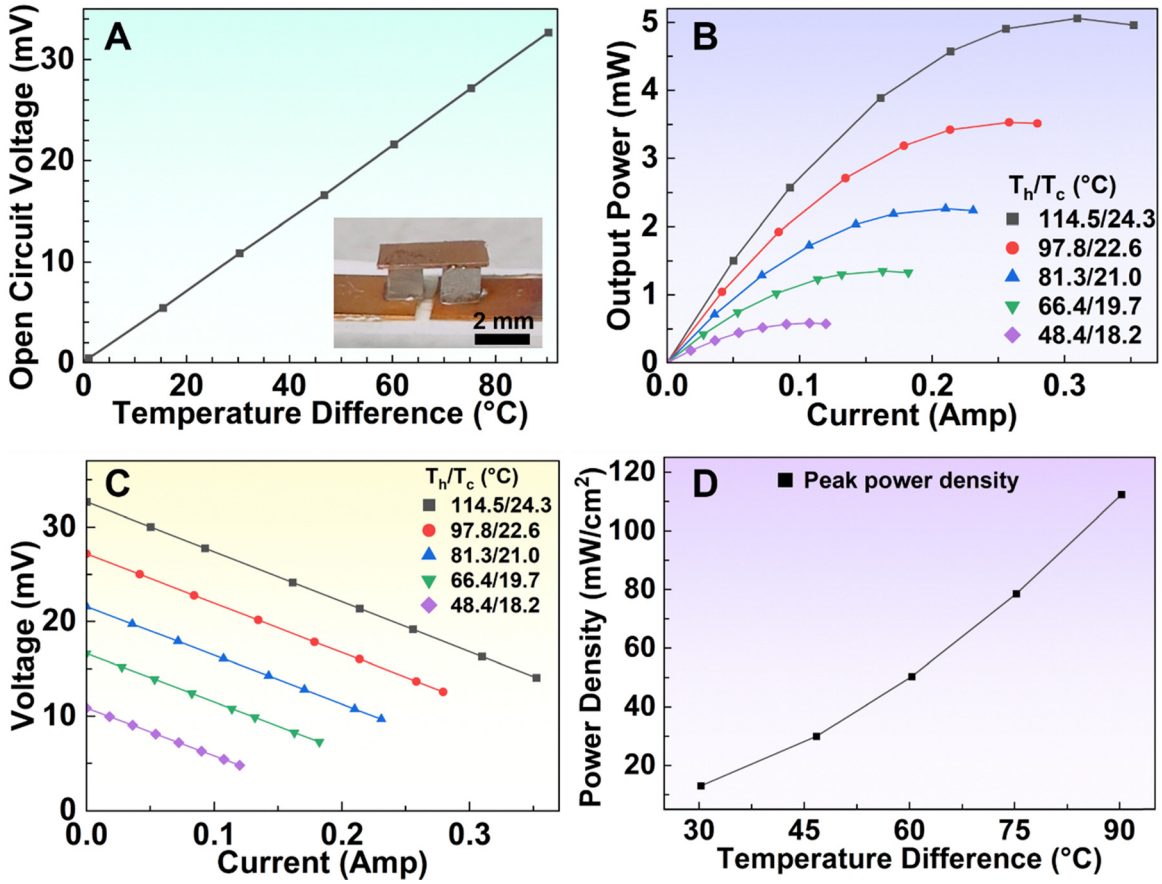

Fig. 4 Power generation performance of the unicouple device: (A) open circuit voltage as a function of temperature difference across the hot side and cold side of the device, the inset image shows the fabricated TEG, (B) output power *vs.* current at different temperature gradients where T_h and T_c denote the hot-side and cold-side temperatures respectively, (C) voltage *vs.* current plot, and (D) peak output power density as a function of temperature difference.

ink was introduced into the PDMS channels, followed by a stainless-steel blade drawing to ensure uniform filling. After removing the mold, the patterned ink retained the cuboid geometry of the template. The coated structures were dried in a vacuum oven (MTI Corporation) at 100 °C for 6 h and synthesized in a tube furnace (GSL1100X, MTI Corporation) under forming gas at controlled temperatures and optimized durations. Densification was achieved by cold pressing at 25 MPa for 10 min. The pressed samples were subsequently sintered in a tube furnace under forming gas, without pressure, to obtain the final thermoelectric structures. The optimized sintering condition was 375 °C for 60 min. Images of the samples after blade-coating and sintering are shown in Fig. S11.

Machine learning modeling and optimization

Finding high-performance materials is challenging because researchers must test numerous combinations of parameters, and experiments are both expensive and time-consuming. This is where a strategic, data-driven approach can provide a significant advantage.[48,49]

To address this challenge, Gaussian Process Regression (GPR) combined with Bayesian Optimization (BO) is often used to guide an adaptive, data-efficient exploration of the parameter space toward optimal material properties.[50,51] Such GPR–BO frameworks have been extensively applied in materials informatics to optimize synthesis conditions and improve target properties.[12,32,34,52,53] Since this framework relies on tunable processing inputs rather than specific chemical assumptions, it is highly generalizable and can be seamlessly adapted to optimize the synthesis parameters of other materials. This application guides the experimental synthesis and maximization of the thermoelectric power factor. This optimization process has three controllable parameters: excess selenium percentage (x_{i1}), synthesis temperature (x_{i2}), and sintering temperature (x_{i3}). The focus of this optimization is to maximize the power factor (y_i). These parameters were explored within physically constrained bounds: excess selenium [0.03,0.20], synthesis temperature [300,400], and sintering temperature [200,450]. The set of N experimental observations is collected in the dataset as $\mathbb{D} = \{(x_i, y_i)|x_i \in \mathbb{R}^3, i \in 1, \ldots, N\}$, abbreviated as $\mathbb{D} = \{X, y\}$.

The relationship between the input parameters and the power factor is treated as an unknown objective function $f(x)$. We place a Gaussian Process (GP) prior over this function. A GP defines a distribution over functions and can be specified by a mean function $m(x)$ and a covariance kernel $k(x,x')$:

$$f(x) \sim \mathrm{GP}(m(x),k(x,x'))$$

The kernel we used is constructed from several components:

$$K(x,x'|\theta) = \text{constant}^2 \times K_{\text{Matern}}(x,x_*|l,\nu) + \sigma^2$$

The hyperparameters were optimized by maximizing the log-marginal likelihood of the training data. These include the constant^2 = 1.33^2, length scale l = [2.3,0.972,1.97], smoothness parameter for the Matern kernel ν = 1, and σ^2 = 0.0003 is the noise level. This kernel provides GPR flexibility and the ability to model complex data relationships. The constant is the scale factor that controls the overall variability; the Matern kernel accommodates functions of moderate roughness, and the white noise term models independent measurement errors. The GPR model utilizes this kernel to describe a joint multivariate Gaussian distribution between training data and prediction points. The covariance matrices derived from the kernel with the training data X, the prediction point x_* are denoted by:

$$\begin{bmatrix} f(X) \\ f(x_*) \end{bmatrix} \sim N\left(\begin{bmatrix} m(X) \\ m(x_*) \end{bmatrix}, \begin{bmatrix} K(X,X) & K(X,x_*) \\ K(x_*,X) & k(x_*,x_*) \end{bmatrix}\right)$$

From the joint Gaussian distribution of training and prediction points, the prediction mean of the power factor $\mu_*(x_*)$ for a given set of input conditions, x_*, and the prediction's uncertainty $\sigma_*(x_*)$ can be derived analytically:

$$\mu_*(x_*) = E(f(x_*)|y) = m(x_*) + K(x_*,X)[K(X,X) + \sigma^2 I]^{-1}\,(y - m(X))$$

$$\sigma_*(x_*) = \text{Var}(f(x_*)|y) = k(x_*,x_*) - K(x_*,X)[K(X,X) + \sigma^2 I]^{-1}K(X,x_*))$$

The GPR model was evaluated using leave-one-out cross-validation (LOOCV). In this procedure, each experiment in the dataset is, in turn, removed from the training set and used as a single-test sample. At the same time, the model is fitted to the remaining $N - 1$ observations. This is repeated over all N data points, and prediction error metrics (RMSE, MAE, R^2) are computed by averaging across all N runs. LOOCV thus ensures maximal usage of the available data for training while assessing generalization performance.

The resulting evaluation yielded RMSE = 0.195 mW m^{-1} K^{-2}, MAE = 0.136 mW m^{-1} K^{-2}, and R^2 = 0.711. The average predicted uncertainty from the model was ±0.198 mW m^{-1} K^{-2}. The synthesis and measurement processes inherently introduce stochastic noise, with our average experimental uncertainty being approximately ±0.127 mW m^{-1} K^{-2}. Because the model's RMSE is on the same order as this fundamental experimental noise floor, the GPR model captures the dominant processing-property trends without overfitting to the experimental data. These results indicate that the model explains approximately 71% of the variance in the power factor, providing reasonable predictive capability, although confidence varies across the parameter space. The corresponding parity plot, shown in Fig. S6, visualizes predicted *versus* experimental power factors across all samples.

Bayesian optimization uses the GP model within an iterative framework to select new experiments. In this case, we use the Expected Improvement (EI) acquisition function to rank candidate points in their potential to outperform the best result observed so far. EI can balance between exploration and exploitation by estimating the expected magnitude of improvement each new test point could offer over the current optimum. EI at the point x_* is calculated as $\text{EI}(x) = \mathbb{E}[\max(f(x_*) - f(x^+), 0]$, where x^+ representing the highest observed power factor input in the current dataset. Under the GP model, $f(x_*)$ follows the Gaussian distribution with mean $\mu_*(x_*)$ and variance $\sigma_*(x_*)$, allowing EI to be expressed analytically:

$$\text{EI}(x_*) = \begin{cases} (\mu_*(x_*) - f(x^+) - \xi)\Phi(z(x_*)) & \\ \quad +\sigma_*(x_*)\phi(z(x_*)), & \sigma_*(x_*) > 0 \\ 0, & \text{otherwise} \end{cases}$$

$$z(x_*) = \begin{cases} \dfrac{(\mu_*(x_*) - f(x^+) - \xi)}{\sigma_*(x_*)}, & \sigma_*(x_*) > 0 \\ 0, & \text{otherwise} \end{cases}$$

where ξ is a positive number to encourage exploration, Φ and ϕ are the cumulative distribution (CDF) and probability density distribution (PDF) of the normal distribution.

The overall optimization workflow, including data normalization, GPR training, EI evaluation, and expert-guided experiment selection, is shown in Fig. S12. Fig. S13 and S14 illustrate how the EI landscape evolves with each optimization round.

Measurement of thermoelectric properties

The room temperature Seebeck coefficient and electrical conductivity were measured using a custom-designed apparatus on freestanding thermoelectric films (Fig. S15). For Seebeck measurements, a temperature gradient of 5 K was applied across the film, and the induced voltage and corresponding temperatures were recorded using k-type thermocouples (Omega, 5TC, 40 AWG). The Seebeck coefficient was determined as $S = -\Delta V/\Delta T$. Electrical conductivity was measured by a standard four-probe method, and high-temperature measurements were performed in ZEM-3 equipment (Ulvac Riko, Japan). Film thickness after sintering was precisely measured using a 2D profilometer (DektakXT, Bruker) with a 0.2 μm stylus under a 1 mg applied force. The measurement uncertainty of the in-house setup was estimated to be ≈5% for both the Seebeck coefficient and conductivity. Thermal conductivity was calculated from $\kappa = \alpha\rho C_p$, where α denotes the thermal diffusivity, ρ is mass density, and C_p represents specific heat. In-plane thermal diffusivity was measured *via* the Angström method by applying a sinusoidal heat signal to one end of the sample using a function generator (RIGOL DG4062) and monitoring the resulting temperature oscillations at two locations along the film (Fig. S8). The phase difference and amplitude ratio of the sinusoidal temperature response were analyzed to extract α following established procedures in the literature.[12] The sample density (7040 Kg m^{-3}) was determined from the measured weight and geometric volume, while C_p values were taken from previously published data.[47] The error in thermal conductivity measurement was estimated to be ≈10%.

Hall effect measurement

Carrier mobility and concentration of Ag_2Se_1 films were measured at room temperature using an automated Hall effect system (HL5500PC). Four 10 mm × 10 mm films were measured for each condition, with the four corners (100 μm × 100 μm) sputter-coated (30 nm Au/Pd alloy, 80% Au and 20% Pd) to minimize contact resistance. The samples for Hall effect measurement and the measurement setup are shown in Fig. S16.

Microstructural characterization

Microstructure was characterized using a Helios G4 UX dual-beam SEM with EDAX in both in-plane and cross-sectional directions. Cross-sectional samples were cut, epoxy-embedded, and polished to reveal internal structures. Phase analysis was conducted by X-ray diffraction using a Bruker D8 Discover system.

Thermoelectric device manufacturing and testing

The fabrication process of the rigid thermoelectric device is summarized in Fig. S17. Silver selenide ink was blade-coated, dried, synthesized, pressed, and sintered to produce disks of 1.5 mm final thickness, which were metalized on both sides to prevent diffusion and reduce contact resistance. A contact layer consisting of 300–400 nm of Ni, followed by ~50 nm of Au, was deposited by an electron beam vacuum deposition system (FC1800-1 Evaporator). The disks were then diced into 1.5 mm × 1.5 mm × 1.5 mm thermoelectric legs using a low-speed diamond saw (SYJ150, MTI Corporation). A 0.5 mm-thick alumina substrate (PATIKIL, USA) was selected for its electrical insulation and high thermal conductivity, and copper electrodes were bonded to the substrate with silver epoxy (H20E, Epoxy Technology). $Bi_{58}Sn_{42}$ solder paste (Wonderway, Germany) was screen-printed on the electrodes (~0.1 mm thick), the thermoelectric legs were placed, an additional solder layer and upper copper electrode were applied. The assembly was aligned with clips and reflowed at 200 °C in an infrared IC heater (T-962) for 7 min, then cooled to room temperature. We used bismuth antimony telluride-based p-type material (Seebeck coefficient 210 μV K^{-1}, and power factor 2.1 mW m^{-1} K^{-2}) to couple with the fabricated n-type material discussed in this work for the 3D device fabrication. The total resistance of the fabricated device was ~50 mΩ, with each contact contributing ~7.4 mΩ. The whole step-by-step device fabrication process is shown in Fig. S10.

The thermoelectric device was tested in a custom setup (Fig. S18), with a heater applied to the hot side and a copper cold plate interfaced with a chiller (Precision Temperature Control System, ThermoTek) was connected to the device's cold side. Two commercial K-type thermocouples (Omega Engineering) were used to monitor temperatures on both the hot and cold sides. Hot and cold-side temperatures were regulated *via* heater voltage and chiller water temperature control, respectively, with constant water flow ensuring uniform cooling. A DC programmable electronic load was employed to draw current from the device to obtain the voltage–current (*V–I*) and power–current (*P–I*) characteristics curves.

Conflicts of interest

There are no conflicts to declare.

Data availability

The data supporting the findings of this study are available from the corresponding author upon reasonable request.

Supplementary information (SI) is available. See DOI: https://doi.org/10.1039/d6mh00220j.

Acknowledgements

We would like to acknowledge support from the National Science Foundation under award number EEC-2330175 for the Engineering Research Center EARTH, U.S. Department of Energy under award DE-EE0009103, and the NSF SBIR Phase-I under award number 2415650. Work at Northwestern University was supported in part by the U.S. Department of Energy, Office of Science and Office of Basic Energy Sciences under award number DE-SC0024256 (thermoelectric measurements).

References

1 J. He and T. M. Tritt, *Science*, 2017, **357**, eaak9997.
2 A. Elson, R. Tidball and A. Hampson, *Waste heat to power market assessment*, Oak Ridge National Lab.(ORNL), Oak Ridge, TN (United States). Building, 2015.
3 A. I. Hochbaum, R. Chen, R. D. Delgado, W. Liang, E. C. Garnett, M. Najarian, A. Majumdar and P. Yang, *Nature*, 2008, **451**, 163–167.
4 J. Mao, G. Chen and Z. Ren, *Nat. Mater.*, 2021, **20**, 454–461.
5 Y. Li, Q. Lou, J. Yang, K. Cai, Y. Liu, Y. Lu, Y. Qiu, Y. Lu, Z. Wang and M. Wu, *Adv. Funct. Mater.*, 2022, **32**, 2106902.
6 K. Song, A. N. M. Tanvir, M. O. Bappy and Y. Zhang, *Small Sci.*, 2025, **5**, 2300359.
7 C. Jiang, P. Wei, Y. Ding, K. Cai, L. Tong, Q. Gao, Y. Lu, W. Zhao and S. Chen, *Nano Energy*, 2021, **80**, 105488.
8 D. Ding, F. Sun, F. Xia and Z. Tang, *Nanoscale Adv.*, 2020, **2**, 3244–3251.
9 G. J. Snyder and E. S. Toberer, *Nat. Mater.*, 2008, **7**, 105–114.
10 Q. Yang, S. Yang, P. Qiu, L. Peng, T.-R. Wei, Z. Zhang, X. Shi and L. Chen, *Science*, 2022, **377**, 854–858.
11 W. Shang, M. Zeng, A. N. M. Tanvir, K. Wang, M. Saeidi-Javash, A. Dowling, T. Luo and Y. Zhang, *Adv. Mater.*, 2023, **35**, 2212230.
12 M. Saeidi-Javash, K. Wang, M. Zeng, T. Luo, A. W. Dowling and Y. Zhang, *Energy Environ. Sci.*, 2022, **15**, 5093–5104.
13 I. T. Witting, T. C. Chasapis, F. Ricci, M. Peters, N. A. Heinz, G. Hautier and G. J. Snyder, *Adv. Electron. Mater.*, 2019, **5**, 1800904.
14 Z. Chen, H. Lv, Q. Zhang, H. Wang and G. Chen, *Carbon Energy*, 2022, **4**, 115–128.
15 Y. Yu, M. Cagnoni, O. Cojocaru-Mirédin and M. Wuttig, *Adv. Funct. Mater.*, 2020, **30**, 1904862.

16 S. Xu, S. Horta, A. Lawal, K. Maji, M. Lorion and M. Ibáñez, *Science*, 2025, **387**, 845–850.
17 Y. Lu, Y. Qiu, K. Cai, Y. Ding, M. Wang, C. Jiang, Q. Yao, C. Huang, L. Chen and J. He, *Energy Environ. Sci.*, 2020, **13**, 1240–1249.
18 S. Jo, S. Cho, U. J. Yang, G. S. Hwang, S. Baek, S. H. Kim, S. H. Heo, J. Y. Kim, M. K. Choi and J. S. Son, *Adv. Mater.*, 2021, **33**, 2100066.
19 Y. Ding, Y. Qiu, K. Cai, Q. Yao, S. Chen, L. Chen and J. He, *Nat. Commun.*, 2019, **10**, 841.
20 T. R. Wei, P. Qiu, K. Zhao, X. Shi and L. Chen, *Adv. Mater.*, 2023, **35**, 2110236.
21 M. Zhu, X.-L. Shi, H. Wu, Q. Liu and Z.-G. Chen, *Chem. Eng. J.*, 2023, **473**, 145236.
22 S. I. Kim, K. H. Lee, H. A. Mun, H. S. Kim, S. W. Hwang, J. W. Roh, D. J. Yang, W. H. Shin, X. S. Li and Y. H. Lee, *Science*, 2015, **348**, 109–114.
23 M. R. Burton, S. Mehraban, D. Beynon, J. McGettrick, T. Watson, N. P. Lavery and M. J. Carnie, *Adv. Energy Mater.*, 2019, **9**, 1900201.
24 M. Burton, G. Howells, J. Atoyo and M. Carnie, *Adv. Mater.*, 2022, **34**, 2108183.
25 J. Lee, S. Choo, H. Ju, J. Hong, S. E. Yang, F. Kim, D. H. Gu, J. Jang, G. Kim and S. Ahn, *Adv. Energy Mater.*, 2021, **11**, 2100190.
26 Q. Zhang, K. Deng, L. Wilkens, H. Reith and K. Nielsch, *Nat. Electron.*, 2022, **5**, 333–347.
27 Y. Wang, L. Yang, X. L. Shi, X. Shi, L. Chen, M. S. Dargusch, J. Zou and Z. G. Chen, *Adv. Mater.*, 2019, **31**, 1807916.
28 Y. Lei, R. Qi, M. Chen, H. Chen, C. Xing, F. Sui, L. Gu, W. He, Y. Zhang and T. Baba, *Adv. Mater.*, 2022, **34**, 2104786.
29 D. Yang, X.-L. Shi, M. Li, M. Nisar, A. Mansoor, S. Chen, Y. Chen, F. Li, H. Ma and G. X. Liang, *Nat. Commun.*, 2024, **15**, 923.
30 Y. Han, X. Li, Y. Jin, X. Wang, X. Sun and C. J. An, *Small*, 2024, **20**, 2309863.
31 M. Zeng, Y. Du, Q. Jiang, N. Kempf, C. Wei, M. V. Bimrose, A. Tanvir, H. Xu, J. Chen and D. J. Kirsch, *Nature*, 2023, **617**, 292–298.
32 K. Song, G. Xu, A. N. M. Tanvir, K. Wang, M. O. Bappy, H. Yang, W. Shang, L. Zhou, A. W. Dowling and T. Luo, *J. Mater. Chem. A*, 2024, **12**, 21243–21251.
33 M. Zeng, D. Zavanelli, J. Chen, M. Saeidi-Javash, Y. Du, S. LeBlanc, G. J. Snyder and Y. Zhang, *Chem. Soc. Rev.*, 2022, **51**, 485–512.
34 A. N. M. Tanvir, M. O. Bappy, M. Zeng, W. Shang, K. Wang, K. Song, Y. Liu, E. Isotta, M. G. Kanatzidis and G. J. Snyder, *Energy Environ. Sci.*, 2024, **17**, 4560–4568.
35 Y. Liu, Q. Zhang, A. Huang, K. Zhang, S. Wan, H. Chen, Y. Fu, W. Zuo, Y. Wang and X. Cao, *Nat. Commun.*, 2024, **15**, 2141.
36 M. M. Mallick, A. G. Rösch, L. Franke, S. Ahmed, A. Gall, H. Geßwein, J. Aghassi and U. Lemmer, *ACS Appl. Mater. Interfaces*, 2020, **12**, 19655–19663.
37 D. Palaporn, K. Kurosaki and S. Pinitsoontorn, *Adv. Energy Sustainability Res.*, 2023, **4**, 2300082.
38 T. Varghese, C. Dun, N. Kempf, M. Saeidi-Javash, C. Karthik, J. Richardson, C. Hollar, D. Estrada and Y. Zhang, *Adv. Funct. Mater.*, 2020, **30**, 1905796.
39 F. Kim, B. Kwon, Y. Eom, J. E. Lee, S. Park, S. Jo, S. H. Park, B.-S. Kim, H. J. Im, M. H. Lee, T. S. Min, K. T. Kim, H. G. Chae, W. P. King and J. S. Son, *Nat. Energy*, 2018, **3**, 301–309.
40 S. Kumar, M. Battabyal, K. Sethupathi and D. K. Satapathy, *ACS Appl. Mater. Interfaces*, 2024, **16**, 40848–40857.
41 S. Kumar, M. Tiadi, V. Trivedi, M. Battabyal and D. K. Satapathy, *ACS Appl. Energy Mater.*, 2023, **6**, 10457–10466.
42 Y.-X. Chen, X.-L. Shi, J.-Z. Zhang, M. Nisar, Z.-Z. Zha, Z.-N. Zhong, F. Li, G.-X. Liang, J.-T. Luo and M. Li, *Nat. Commun.*, 2024, **15**, 8356.
43 T. Cao, X.-L. Shi, B. Hu, Q. Yang, W.-Y. Lyu, S. Sun, L.-C. Yin, Q.-Y. Liu, W. Chen and X. Wang, *Nat. Commun.*, 2025, **16**, 1555.
44 P. Jood, R. Chetty and M. Ohta, *J. Mater. Chem. A*, 2020, **8**, 13024–13037.
45 L. Jia, W. Ai, J. Gao, J.-C. Guo, H. Ruan, L. Miao and C. Liu, *ACS Appl. Energy Mater.*, 2024, **7**, 5721–5727.
46 W. Xu, Q. Song, G. Song and Q. Yao, *Thermochim. Acta*, 2020, **683**, 178480.
47 J. Gao, L. Miao, H. Lai, S. Zhu, Y. Peng, X. Wang, K. Koumoto and H. Cai, *IScience*, 2020, **23**, 100753.
48 S. Alosious, M. Jiang and T. Luo, *MRS Bull.*, 2025, 1–13.
49 M. N. Carlozo, K. Wang and A. W. Dowling, *Ind. Eng. Chem. Res.*, 2025, **64**, 18277–18297.
50 K. Wang and A. W. Dowling, *Curr. Opin. Chem. Eng.*, 2022, **36**, 100728.
51 C. Wang, Y.-J. Kim, A. Vriza, R. Batra, A. Baskaran, N. Shan, N. Li, P. Darancet, L. Ward and Y. Liu, *Nat. Commun.*, 2025, **16**, 1498.
52 T. Lookman, P. V. Balachandran, D. Xue and R. Yuan, *npj Comput. Mater.*, 2019, **5**, 21.
53 R. Gómez-Bombarelli, J. N. Wei, D. Duvenaud, J. M. Hernández-Lobato, B. Sánchez-Lengeling, D. Sheberla, J. Aguilera-Iparraguirre, T. D. Hirzel, R. P. Adams and A. Aspuru-Guzik, *ACS Cent. Sci.*, 2018, **4**, 268–276.